

Large anomalous Hall and Nernst effect in the breathing kagome ferromagnet $NdCrGe_3$

Yang Liu(刘洋), Meng Lyu(吕孟), Junyan Liu(刘俊艳), Yibo Wang(王一博), Jinying Yang(杨金颖), Binbin Wang(王彬彬), Xiyang Li(李西阳), and Enke Liu(刘恩克)

Citation: Chin. Phys. B, 2026, 35 (**5**): 057201. DOI: 10.1088/1674-1056/ae44f0
http://cpb.iphy.ac.cn; http://iopscience.iop.org/cpb

What follows is a list of articles you may be interested in

Asymmetric gaps of tetralayer graphene unveiled by thermodynamic characterization

Zhuangzhuang Qu(曲壮壮), Zhuoxian Li(李卓贤), Boxi Li(李博熙), Lipeng Hou(侯立芃), Xiangyan Han(韩香岩), Qianling Liu(刘倩伶), Zhiyu Wang(王知雨), Kenji Watanabe, Takashi Taniguchi, Yanmeng Shi(史衍猛), and Jianming Lu(路建明)

Chin. Phys. B, 2025, 34 (**11**): 117201. DOI: 10.1088/1674-1056/adf9fc

Anomalous Hall effect in Bernal tetralayer graphene enhanced by spin-orbit interaction

Zhuangzhuang Qu(曲壮壮), Zhihao Chen(陈志豪), Xiangyan Han(韩香岩), Zhiyu Wang(王知雨), Zhuoxian Li(李卓贤), Qianling Liu(刘倩伶), Wenjun Zhao(赵文俊), Kenji Watanabe, Takashi Taniguchi, Zhi-Gang Cheng(程智刚), Zizhao Gan(甘子钊), and Jianming Lu(路建明)

Chin. Phys. B, 2025, 34 (**3**): 037201. DOI: 10.1088/1674-1056/adb411

Effect of the mixing of s-wave and chiral p-wave pairings on electrical shot noise properties of normal metal/superconductor tunnel junctions

Yu-Chen Hu(胡雨辰) and Liang-Bin Hu(胡梁宾)

Chin. Phys. B, 2024, 33 (**7**): 077202. DOI: 10.1088/1674-1056/ad498a

Doping tuned anomalous Hall effect in the van der Waals magnetic topological phases $Mn(Sb_{1-x}Bi_x)_4Te_7$

Xin Zhang(张鑫), Zhicheng Jiang(江志诚), Jian Yuan(袁健), Xiaofei Hou(侯骁飞), Xia Wang(王霞),Na Yu(余娜), Zhiqiang Zou(邹志强), Zhengtai Liu(刘正太), Wei Xia(夏威),Zhenhai Yu(于振海), Dawei Shen(沈大伟), and Yanfeng Guo(郭艳峰)

Chin. Phys. B, 2023, 32 (**9**): 097201. DOI: 10.1088/1674-1056/acd629

Strain-dependent resistance and giant gauge factor in monolayer WSe_2

Mao-Sen Qin(秦茂森), Xing-Guo Ye(叶兴国), Peng-Fei Zhu(朱鹏飞), Wen-Zheng Xu(徐文正), Jing Liang(梁晶), Kaihui Liu(刘开辉), and Zhi-Min Liao(廖志敏)

Chin. Phys. B, 2021, 30 (**9**): 097203. DOI: 10.1088/1674-1056/ac11d2

RAPID COMMUNICATION

Large anomalous Hall and Nernst effect in the breathing kagome ferromagnet $NdCrGe_3$

Yang Liu(刘洋)[1,2], Meng Lyu(吕孟)[1], Junyan Liu(刘俊艳)[1], Yibo Wang(王一博)[1,2], Jinying Yang(杨金颖)[1], Binbin Wang(王彬彬)[1], Xiyang Li(李西阳)[1], and Enke Liu(刘恩克)[1,2,†]

[1] *Beijing National Laboratory for Condensed Matter Physics, Institute of Physics, Chinese Academy of Sciences, Beijing* 100190, *China*
[2] *University of Chinese Academy of Sciences, Beijing* 100049, *China*

(Received 29 January 2026; revised manuscript received 29 January 2026; accepted manuscript online 12 February 2026)

The anomalous Hall and Nernst effects provide critical probes for investigating the Berry-curvature-related electronic band characteristics in magnetic materials. In this study, we conducted a comprehensive investigation into the magnetic, electrical, and thermal transport properties of $NdCrGe_3$ single crystals with a Ge-based breathing kagome lattice. This compound undergoes a ferromagnetic transition at 128 K, and magnetic ordering of the Nd sublattice emerges below 100 K. Transport measurements indicate that $NdCrGe_3$ manifests large anomalous Hall conductivity with $\sigma_{xy}^{\mathrm{A}} \approx 380\ \Omega^{-1}\cdot\mathrm{cm}^{-1}$ at low temperatures and an anomalous Nernst coefficient with $|S_{xy}^{\mathrm{A-max}}| = 0.74\ \mu\mathrm{V/K}$ at 100 K. Scaling analysis reveals that $NdCrGe_3$ exhibits large intrinsic anomalous Hall conductivity of $\sim 260\ \Omega^{-1}\cdot\mathrm{cm}^{-1}$ and falls within the intrinsic regime of the unified model. Furthermore, the anomalous Nernst coefficient breaks down the scaling relationship with magnetization observed in conventional ferromagnets, while the anomalous Nernst conductivity manifests a scaling behavior of $T\ln T$. These results demonstrate that the anomalous transverse transport properties of $NdCrGe_3$ are predominantly governed by the intrinsic Berry mechanism.

Keywords: anomalous Hall effect, anomalous Nernst effect, Berry curvature, breathing kagome lattice, $NdCrGe_3$

PACS: 72.15.–v, 72.15.Jf, 75.20.En

DOI: 10.1088/1674-1056/ae44f0 **CSTR:** 32038.14.CPB.ae44f0

1. Introduction

The anomalous Hall effect (AHE) is a significant electronic transport phenomenon in which conduction electrons undergo transverse motion in the absence of an external magnetic field.[1] Conventionally, the AHE is considered to be proportional to the saturation magnetic moment (M_{s}), as described by the relation $\rho_{\mathrm{H}}^{\mathrm{A}} = 4\pi R_{\mathrm{s}} M_{\mathrm{s}}$, where R_{s} is the anomalous Hall coefficient, a parameter linked to the inherent characteristics of materials.[2,3] However, the AHE of some ferromagnetic compounds deviates from this empirical rule. Mn_2CoGa, which has a large saturation magnetic moment of $\sim 2\ \mu_{\mathrm{B}}$/f.u., exhibits an almost zero anomalous Hall conductivity (σ_{xy}^{A}).[4,5] In contrast, a significant AHE is observed in Mn_3X (X = Ge, Sn) with nearly negligible magnetic moment.[6,7] These experimental results demonstrate that M_{s} is not the dominant cause of the AHE. In the last several decades, with further theoretical and experimental research, the AHE has been broadly recognized as arising from two distinct microscopic mechanisms: an intrinsic mechanism associated with Berry curvature (Ω^z) and extrinsic processes arising from scattering.[1,8–13] Among them, the intrinsic mechanism is related to the electronic band structure of the material, with intrinsic anomalous Hall conductivity ($\sigma_{xy}^{\mathrm{A-int.}}$) calculated using the formula[14]

$$\sigma_{ij}^{\mathrm{A}} = \frac{e^2}{\hbar}\sum_n \int \frac{\mathrm{d}^3k}{(2\pi)^3}\Omega_{ij}^n f_n, \tag{1}$$

where f_n is the Fermi distribution, indicating that strong Berry curvature below the Fermi level (E_{F}) could lead to a giant σ_{xy}^{A}. As a thermal analogue of the AHE, the anomalous Nernst effect (ANE) describes the generation of a transverse electric field under a longitudinal temperature gradient in zero magnetic field.[15,16] The ANE is also associated with Ω^z, and the anomalous Nernst conductivity (α_{yx}^{A}) could be calculated using the formula[14,17]

$$\alpha_{ij}^{\mathrm{A}} = -\frac{1}{T}\frac{e}{\hbar}\sum_n \int \frac{\mathrm{d}^3k}{(2\pi)^3}\Omega_{ij}^n \times \left[(E_n - E_{\mathrm{F}})f_n + k_{\mathrm{B}}T\ln\left(1+\exp\frac{E_n - E_{\mathrm{F}}}{-k_{\mathrm{B}}T}\right)\right], \tag{2}$$

reflecting that the ANE is governed by the Berry curvature around E_{F} and is more sensitive to the band structure. On the other hand, it has been established that topological electronic structures, such as Weyl nodes and nodal rings, can generate strong Berry curvature.[18–20] Consequently, giant

†Corresponding author. E-mail: ekliu@iphy.ac.cn

© 2026 Chinese Physical Society and IOP Publishing Ltd. All rights, including for text and data mining, AI training, and similar technologies, are reserved.

AHE and ANE have been extensively observed in magnetic topological materials, including the magnetic Weyl semimetal $Co_3Sn_2S_2$[21,22] and the ferromagnetic nodal-line compound Co_2MnGa.[23,24] Therefore, the anomalous transverse transport phenomena, intrinsically dominated by the Berry curvature, provide an effective tool to probe the topological nature of magnetic materials.

Recently, RTX_3 (R = La–Nd, Sm; T = transition metals; X = group 13–15 elements) compounds, with a rich diversity of crystal structures, have attracted extensive scientific interest due to a wide range of fascinating physical properties, including superconductivity, heavy fermion behavior, and topologically nontrivial states.[25,26] Among them, RCrGe$_3$ compounds crystallizing in a hexagonal lattice structure exhibit a breathing kagome lattice composed of Ge atoms, which might host nontrivial topological states such as Dirac points, flat bands, and Van Hove singularities in the electronic bands.[27–30] Besides, RCrGe$_3$ are reported to be ferromagnets, with Curie temperatures (T_C) ranging from 60 K to 155 K, thus breaking time-reversal symmetry (TRS) and enriching physical properties.[26,31] Furthermore, giant AHE and ANE have been observed in LaCrGe$_3$ and CeCrGe$_3$.[32,33] Considering that the electrical and thermal transport properties of NdCrGe$_3$ single crystals have not yet been investigated, the present study has been undertaken to comprehensively analyze and report on the relevant characteristics.

In this work, NdCrGe$_3$ single crystals were grown using the Ge self-flux method, and the magnetic, electrical, and thermal transport properties were investigated in detail. Magnetization measurements reveal that NdCrGe$_3$ undergoes a ferromagnetic transition at 128 K with the Cr moment aligned along the c-axis, and the Nd moment emerges below 100 K. Electrical and thermal transport measurements show that NdCrGe$_3$ exhibits large AHE and ANE, and further scaling analysis indicates that the prominent anomalous transverse transport properties of NdCrGe$_3$ are dominated by the intrinsic Berry mechanism.

2. Experimental methods

NdCrGe$_3$ single crystals were grown using the high-temperature Ge self-flux method.[34] The initial elements of high-purity Nd (ingots, 99.9%), Cr (pieces, 99.99%), and Ge (pieces, 99.999%) were weighed and combined in a molar ratio of 13:13:74. Then, the mixture was placed in an alumina crucible and sealed in a quartz tube under the partial pressure of high-purity argon gas. The quartz tube was heated to 1100 °C in 12 h and kept for 24 h, then slowly cooled to 850 °C over a week. Finally, the remaining liquid was decanted using a centrifuge to obtain hexagonal prism-shaped NdCrGe$_3$ single crystals, as shown in the inset of Fig. 1(d).

The chemical composition and homogeneity of the as-grown crystals were analyzed using a Hitachi S-4800 scanning electron microscope (SEM) with energy-dispersive x-ray spectroscopy (EDS). The single-crystal structure was determined by x-ray diffraction (XRD) on a Rigaku D/Max-2400 diffractometer at room temperature using Cu K_α radiation ($\lambda = 0.71073$ Å). Additionally, the crystal orientation was verified on a Bruker D2 Phaser under the same experimental conditions.

The electrical transport measurements were carried out in the physical property measurement system (PPMS, Quantum Design) over a temperature range from 2 K to 300 K. The standard six-probe method was used to measure the longitudinal (ρ_{xx}) and Hall (ρ_{yx}) resistivities. The thermoelectric measurements, including the Seebeck (S_{xx}) and Nernst (S_{yx}) coefficients, were carried out in the PPMS under high vacuum. To isolate the intrinsic signal from contributions arising from electrode misalignment, the four above-mentioned parameters were measured by scanning both negative and positive magnetic fields, and the experimental data sets were then processed using standard symmetry operations to separate the symmetric and antisymmetric components.

3. Results and discussion

The bulk NdCrGe$_3$ crystallizes in a $BaNiO_3$-type structure with the space group $P6_3/mmc$ (No. 194),[31] as shown on the left of Fig. 1(a). The orange, mazarine, and purple spheres represent Nd, Cr, and Ge atoms, respectively. In the ground state, the magnetic moments of Nd and Cr are aligned along the c-axis.[35] Furthermore, Ge atoms form a breathing kagome lattice, which is composed of corner-sharing triangles with unequal Ge–Ge bond lengths, as illustrated on the right of Fig. 1(a). By breaking the sixfold symmetry of a normal kagome lattice, the breathing configuration potentially hosts richer physical phenomena.[28] The EDS results show that the ratio of Nd:Cr:Ge is close to 1:1:3, and the elemental mapping validates the homogeneous distribution of Nd, Cr, and Ge, as depicted in Fig. 1(b). The powder XRD pattern of NdCrGe$_3$ can be accurately refined using the $BaNiO_3$-type structure in Fig. 1(c), yielding lattice parameters of $a = b = 6.147$ Å and $c = 5.720$ Å, which are consistent with previous reports.[31] The single-crystal XRD pattern in Fig. 1(d) shows that the exposed crystal plane of the sample (see the inset figure) corresponds to the (100) plane.

As illustrated in Figs. 2(a) and 2(d), the magnetization increases sharply around 128 K, suggesting that the Curie temperature (T_C) of NdCrGe$_3$ is 128 K. The c-axis is identified as the easy magnetization direction of NdCrGe$_3$, as evidenced by a comparison of the results presented in Figs. 2(b) and 2(e). Furthermore, as demonstrated in Fig. 2(a), the magnetic susceptibility undergoes a further increase below T_C in the field-

cooling (FC) mode with $H \parallel c$, which is attributed to the onset of the Nd moment. The initiation and termination temperatures are denoted as T_{C1}^{Nd} ($\sim$ 100 K) and T_{C2}^{Nd} ($\sim$ 20 K), respectively. This finding is consistent with the results of the isothermal magnetization curves in Fig. 2(b). The magnetization reaches a saturation value of $M_s = 1.18$ μ_B/f.u. at 120 K, which is essentially identical to the Cr-only moment reported for $LaCrGe_3$ ($M_s \approx 1.25$ μ_B/Cr at 2 K).[34] Consequently, at this temperature, the magnetization is attributable solely to the Cr sublattice. As the temperature decreases further, the saturation moment increases to a maximum value of approximately 3.15 μ_B/f.u. below 20 K, which reflects the fact that the Nd contribution is equivalent to $M_s \approx 1.97$ μ_B/Nd in $NdCrGe_3$. The magnetization curves show the distinctive hysteresis of a hard ferromagnet. The coercive field is as large as 0.72 T at 2 K, decreasing monotonically with increasing temperature, as illustrated in Fig. 2(c).

Figure 2(e) shows the isothermal magnetization curves with $H \parallel ab$, which present more complex magnetic behavior compared with those of $H \parallel c$. It is demonstrated that a hard-magnetic hysteresis loop manifests at low fields (i.e., below 20 K), while a metamagnetic transition becomes evident at high fields (i.e., below 100 K). It is noted that the metamagnetic field at 2 K is higher than the largest measured field (9 T). Furthermore, it is observed that the metamagnetic transition vanishes at 100 K, a temperature (T_{C1}^{Nd}) at which the Nd moment emerges, as demonstrated in Fig. 2(f). Evidently, the occurrence of the metamagnetic transition can be attributed to the f electrons of Nd, thereby underlining the delicate interplay between the Cr-derived itinerant magnetism and the localized Nd f-moment in $NdCrGe_3$.

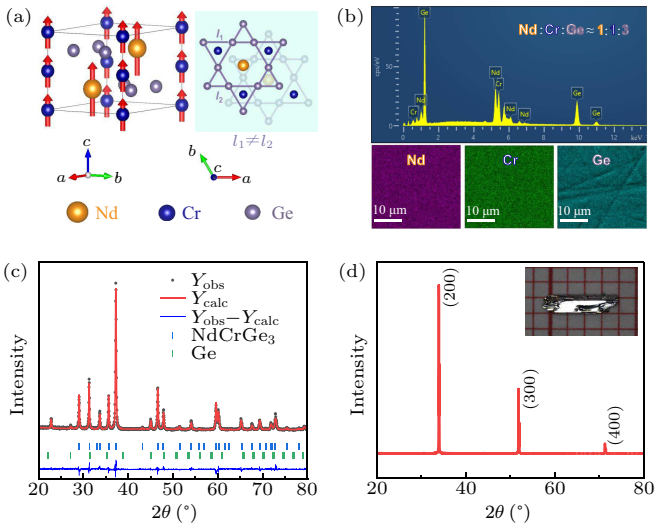


Fig. 1. Structure and chemical composition of $NdCrGe_3$. (a) Crystal structure. The left image shows that the magnetic moments of Nd and Cr align along the *c*-axis. The right image shows a breathing kagome lattice composed of Ge atoms within the *ab*-plane. (b) EDS result. (c) Refined powder XRD pattern recorded at room temperature. (d) Single-crystal XRD pattern. The inset is an image of $NdCrGe_3$ single crystal.

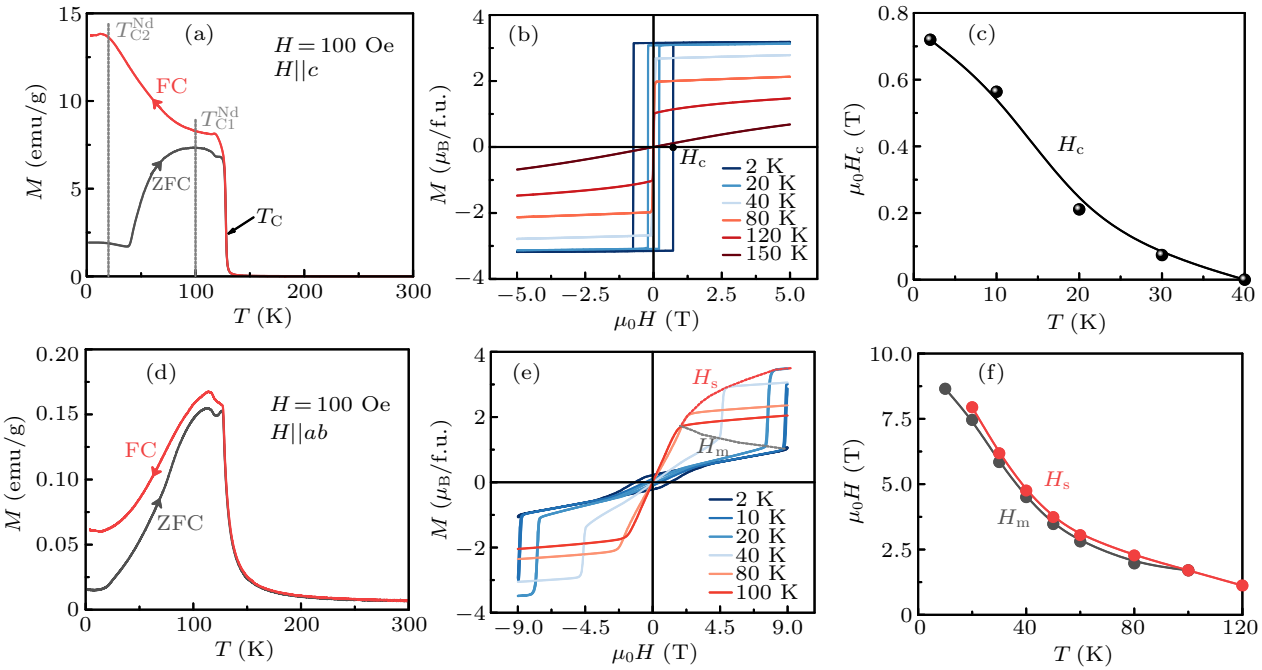


Fig. 2. Magnetic properties of $NdCrGe_3$. (a) and (d) Temperature dependence of the magnetic susceptibility with $H \parallel c$ and $H \parallel ab$ at 100 Oe, respectively. (b) and (e) Isothermal magnetization curves at different temperatures with $H \parallel c$ and $H \parallel ab$, respectively. (c) Temperature dependence of the coercive field (H_c) with $H \parallel c$. (f) Temperature dependence of the metamagnetic field (H_m) and the saturation field (H_s) with $H \parallel ab$. H_m and H_s exhibit a shift toward lower values upon warming.

To elucidate the properties of $NdCrGe_3$ further, we carried out comprehensive electrical and thermal transport measurements. Figure 3(a) presents the temperature-dependent resistivity (ρ_{xx}) measured in both zero field and a field of 9 T, and the inset provides a visual representation of the measurement configuration with $I \parallel a$ and $H \parallel c$. The zero-field ρ_{xx}

demonstrates metallic behavior, exhibiting a linear decrease from room temperature down to T_C, below which it experiences a sharp decline. The sharp downturn observed in the data signifies the suppression of spin-dependent scattering. The additional reduction of ρ_{xx} around T_C under a field of 9 T further corroborates the pivotal role of spin-dependent scattering in governing the resistivity. In addition, the residual resistivity is 150.09 μΩ·cm at 2 K, and the residual resistivity ratio (RRR) is found to be approximately 1.8, evaluated by RRR = ρ(300 K)/ρ(2 K). The value falls within the lower range, which is of the same order of magnitude as that of $LaCrGe_3$.[32]

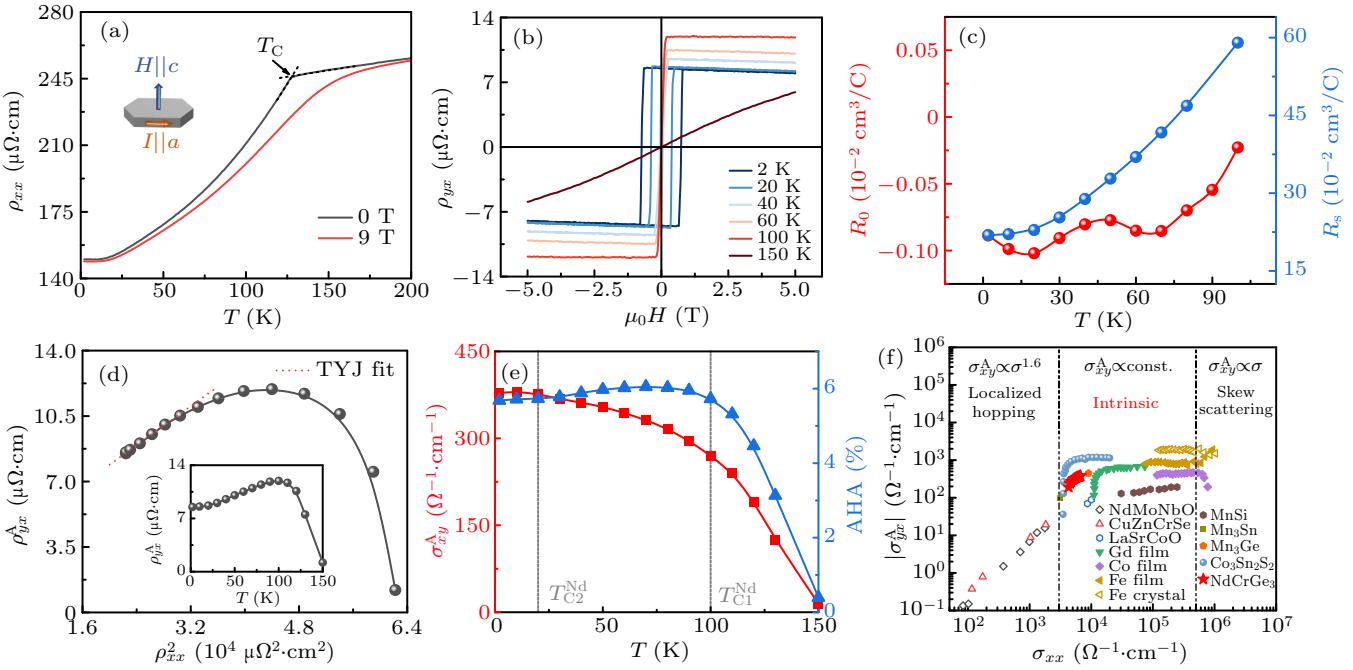


Fig. 3. Electrical transport properties of $NdCrGe_3$. (a) Temperature dependence of the longitudinal resistivity (ρ_{xx}) in zero field and a field of 9 T. The inset shows the measurement configuration with $I \parallel a$ and $H \parallel c$. (b) Field dependence of the Hall resistivity (ρ_{yx}) at various temperatures. (c) Temperature dependence of the normal Hall coefficient (R_0) and the anomalous Hall coefficient (R_s). (d) The relationship between ρ^A_{yx} and ρ^2_{xx}. The inset shows the temperature-dependent anomalous Hall resistivity (ρ^A_{yx}). (e) Temperature dependence of the anomalous Hall conductivity (σ^A_{xy}) and the anomalous Hall angle (AHA). (f) Unified model of σ^A_{xy} as a function of σ_{xx} for different magnetic materials. The σ^A_{xy} is extracted below T_C in $NdCrGe_3$.

As illustrated in Fig. 3(b), the field-dependent Hall resistivity (ρ_{yx}) of $NdCrGe_3$ from 2 K to 150 K displays a clearly defined rectangular hysteresis loop, which is indicative of the AHE. In general, the Hall resistivity can be expressed as[1]

$$\rho_{yx} = \rho^N_{yx} + \rho^A_{yx} = R_0 B + 4\pi R_s M, \tag{3}$$

where R_0 and R_s represent the normal and anomalous Hall coefficients, respectively. The obtained parameters R_0 and R_s are depicted in Fig. 3(c). The negative R_0 below 100 K signifies the dominant presence of electron-type carriers within the band structures, and further calculations reveal that the carrier density of $NdCrGe_3$ is estimated to be $n_e \approx 10^{21}$ cm^{-3}, which falls within the boundary region between metals and semimetals. The large R_s indicates the predominant anomalous Hall effect in $NdCrGe_3$, which is approximately two orders of magnitude greater than R_0. The temperature-dependent anomalous Hall resistivity (ρ^A_{yx}) can be obtained by estimating the high-field linear component of ρ_{yx} at different temperatures, as shown in the inset of Fig. 3(d). It is evident that ρ^A_{yx} exhibits an initial increase followed by a subsequent decrease in response to increasing temperature, attaining a maximum value of 11.9 μΩ· cm at 100 K. Furthermore, the anomalous Hall conductivity (σ^A_{xy}) is calculated using the equation

$$\sigma^A_{xy} = \frac{\rho^A_{yx}}{\rho^2_{xx} + (\rho^A_{yx})^2}. \tag{4}$$

Here, ρ_{xx} is estimated by the zero-field value. As depicted in Fig. 3(e), σ^A_{xy} maintains a comparatively substantial constant value of $\sim$ 380 Ω^{-1}·cm^{-1} below T^{Nd}_{C2} when the magnetic order stabilizes, and σ^A_{xy} undergoes a gradual decline as the temperature rises. The intrinsic anomalous Hall conductivity ($\sigma^{A-int.}_{xy}$) could be obtained in Fig. 3(d) by applying the TYJ scaling model[36]

$$\rho_{AH} = (\alpha\rho_{xx0} + \beta\rho^2_{xx0}) + b\rho^2_{xx}, \tag{5}$$

where the fitting range is below T^{Nd}_{C2}. Here, ρ_{xx0} is the residual resistivity, and $b\rho^2_{xx}$ represents the intrinsic contribution. The result of the fitting process indicates that $\sigma^{A-int.}_{xy}$ is $\sim$ 260 Ω^{-1}·cm^{-1}, which can be ascribed to the presence of relatively strong Berry curvature. The intrinsic value is approximately 70% of the total σ^A_{xy}, indicating that the intrinsic Berry curvature dominates the anomalous Hall effect of

$NdCrGe_3$. Additionally, it is noteworthy that no substantial alterations of σ_{xy}^{A} are observed following the emergence of the Nd moment in Fig. 3(e). Since the intrinsic AHE is related to the Berry curvature arising from the energy bands, the observation suggests that Nd bands contribute little to the Berry curvature responsible for generating σ_{xy}^{A}, which might be attributed to the relatively narrow width of Nd bands and their greater distance from E_F. As demonstrated in Fig. 3(e), the anomalous Hall angle (AHA) of $NdCrGe_3$ manifests a relatively large constant value (~ 6 %) below T_{C1}^{Nd}, calculated by

$$\mathrm{AHA} = \frac{\rho_{yx}^{A}}{\rho_{xx}}. \tag{6}$$

Furthermore, the data of $NdCrGe_3$ were incorporated into the unified model for analysis,[37,38] with the absolute amplitudes of σ_{xy}^{A} plotted against the conductivity (σ_{xx}) in Fig. 3(f). Apparently, σ_{xx} of $NdCrGe_3$ ($\sim 10^5$ $\Omega^{-1}\cdot cm^{-1}$) falls into the intrinsic regime with $\sigma_{xx} \sim 10^4$–10^6 $\Omega^{-1}\cdot cm^{-1}$, and in this regime, σ_{xy}^{A} remains constant in the presence of changes to σ_{xx}. This provides the information that $NdCrGe_3$ exhibits relatively large Berry curvature. Meanwhile, compared to $LaCrGe_3$,[32] $NdCrGe_3$ incorporates f-electrons, resulting in richer magnetic behavior. However, the order of magnitude of σ_{xy}^{A} in the two compounds remains approximately the same, suggesting that the Cr magnetic moment primarily contributes to the intrinsic AHE. In contrast to the previous two compounds, $CeCrGe_3$ exhibits strong electronic correlations that may induce band renormalization, thereby enhancing the Berry curvature of energy bands; consequently, $CeCrGe_3$ exhibits a significantly giant AHE.[33]

Furthermore, thermoelectric measurements provide a powerful means to probe the intrinsic transport properties of materials. Accordingly, the Seebeck and Nernst effects of $NdCrGe_3$ were carried out in the configuration with $-\nabla T \parallel a$ and $H \parallel c$, as illustrated in the inset of Figs. 4(a) and 4(b). In Fig. 4(a), a distinctive kink is observed around T_C in the zero-field Seebeck coefficient (S_{xx}) curve, indicating the occurrence of a ferromagnetic phase transition. It is noteworthy that the signs of S_{xx} and R_0 appear mismatched below T_C. In magnetic materials, the contribution from spin entropy or magnetic drag may provide a significant component to S_{xx}, potentially dominating the carrier contribution.[39] This could lead to S_{xx} maintaining positive values below T_C in $NdCrGe_3$.

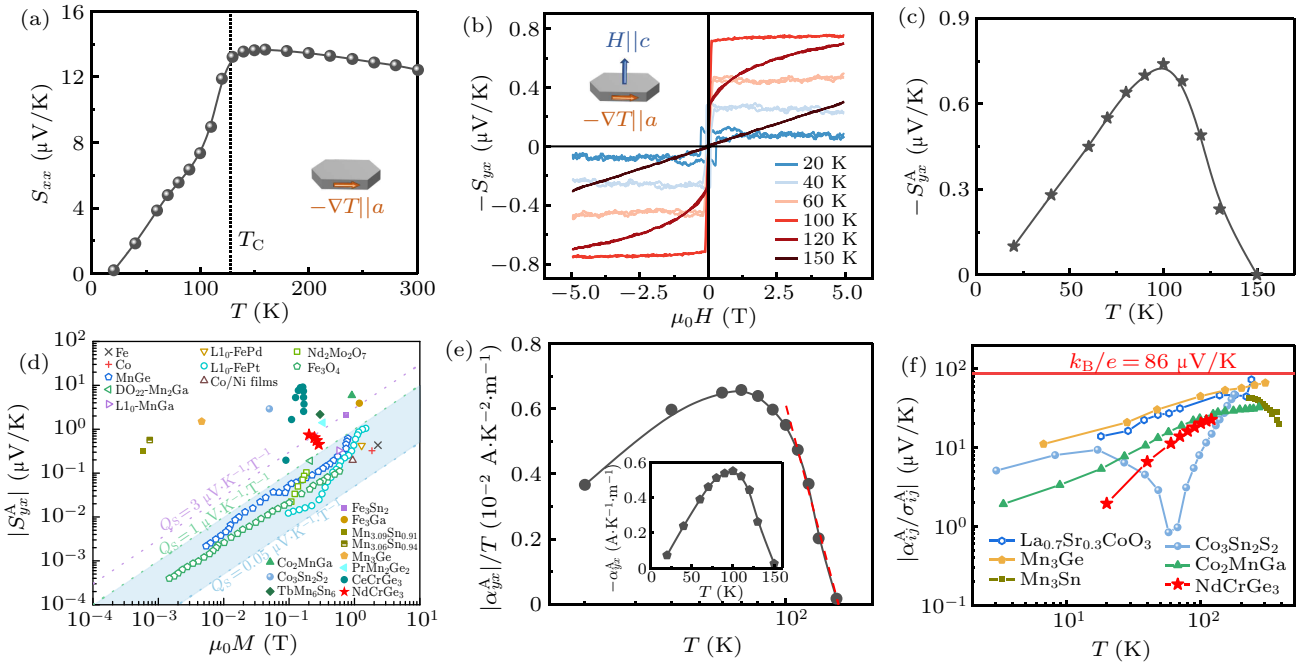


Fig. 4. Thermal transport properties of $NdCrGe_3$ crystals. (a) Temperature dependence of the Seebeck coefficient (S_{xx}) in zero field. The inset shows the measurement configuration with $-\nabla T \parallel a$. (b) Magnetic field dependence of the Nernst coefficient (S_{yx}) at different temperatures. The inset shows the measurement configuration with $-\nabla T \parallel a$ and $H \parallel c$. (c) Temperature dependence of the anomalous Nernst coefficient (S_{yx}^{A}). (d) Magnetization dependence of $|S_{yx}^{A}|$ for different magnetic materials. It is observed that $NdCrGe_3$ is located outside the conventional ferromagnets regime, which is marked by light blue. (e) $|\alpha_{yx}^{A}|/T$ as a function of temperature. The inset shows the temperature-dependent anomalous thermoelectric conductivity (α_{yx}^{A}). (f) Temperature dependence of the ratio $|\alpha_{ij}^{A}/\sigma_{ij}^{A}|$ for different magnetic topological materials. The α_{xy}^{A} is extracted below T_C in $NdCrGe_3$, and the red solid line represents the value of k_B/e.

The Nernst coefficient (S_{yx}) of $NdCrGe_3$ exhibits a distinct hysteresis loop at low fields and saturates at high fields, as demonstrated in Fig. 4(b). Analogous to the Hall effect, the total Nernst signal comprises the normal and anomalous contributions[40]

$$S_{yx} = S_{yx}^{N} + S_{yx}^{A} = Q_0 H + Q_s \mu_0 M, \tag{7}$$

where Q_0 and Q_s represent the normal and anomalous Nernst

coefficients, respectively. The symbol μ_0 denotes the vacuum permeability, which is a fundamental concept in the field of electromagnetism. The anomalous Nernst coefficient $|S_{yx}^{A}|$ attains a maximal value of 0.74 $\mu V \cdot K^{-1}$ at 100 K in Fig. 4(c), which is considerably larger than that observed in conventional ferromagnetic materials (i.e., Fe and Co,[41] as well as the ferrite Fe_3O_4[42]). Moreover, a comparison of the magnetization-dependent S_{yx}^{A} across several materials[33,43] is outlined in Fig. 4(d). The Q_s of $NdCrGe_3$ is as high as 3 $\mu V \cdot K^{-1} \cdot T^{-1}$, surpassing the threshold of the scaling regime of conventional ferromagnets (0.05 $\mu V \cdot K^{-1} \cdot T^{-1} \leq Q_s \leq 1.0$ $\mu V \cdot K^{-1} \cdot T^{-1}$),[40] which reveals that $NdCrGe_3$ exhibits a relatively large Berry curvature compared to conventional ferromagnets.

In order to achieve a more profound comprehension of the intrinsic ANE, the thermoelectric conductivity (α_{yx}^{A}) can be calculated through the equation[44]

$$\alpha_{yx}^{A} = \sigma_{xx} S_{yx}^{A} - \sigma_{xy}^{A} S_{xx}. \tag{8}$$

As illustrated in the inset of Fig. 4(e), α_{yx}^{A} of $NdCrGe_3$ is obtained, with an absolute maximum value of 0.55 $A \cdot K^{-1} \cdot m^{-1}$ at 100 K. Moreover, the temperature dependence of $\left|\alpha_{yx}^{A}\right|/T$ below T_C is exhibited in Fig. 4(e), demonstrating a distinctive scaling behavior of $T \ln T$ above 100 K. This phenomenon indicates that the presence of large ANE stems from the relatively strong Berry curvature.[44,45] Furthermore, we systematically compared the ratio of $|\alpha_{ij}^{A}|/|\sigma_{ij}^{A}|$ with some novel magnetic materials in Fig. 4(f). It can be posited that the ratio of $NdCrGe_3$ approaches a saturation value of $k_B/e = 86$ $\mu V \cdot K^{-1}$, which has been observed in materials exhibiting strong Berry curvature.[45,46] This provides further evidence that the anomalous transverse transport properties of $NdCrGe_3$ stem from relatively large Berry curvature.

4. Conclusion

We have successfully grown $NdCrGe_3$ single crystals using the Ge self-flux method and carried out systematic investigations of their magnetic and transport properties. $NdCrGe_3$ adopts a hexagonal $BaNiO_3$-type structure with a breathing kagome lattice of Ge atoms, and the ferromagnetic ordering of $NdCrGe_3$ at 128 K is characterized by magnetic susceptibility, electrical resistivity, and Seebeck coefficient measurements. Remarkably, $NdCrGe_3$ exhibits a large AHE of 380 $\Omega^{-1} \cdot cm^{-1}$ at low temperatures and an ANE of 0.74 $\mu V \cdot K^{-1}$ at 100 K, accompanied by typical hysteresis loops. Further scaling analysis demonstrates that the anomalous transverse transport properties of $NdCrGe_3$ are primarily dominated by relatively strong Berry curvature arising from the electronic bands. Furthermore, theoretical calculations and spectroscopic experiments are required to clarify the electronic band structure of $NdCrGe_3$.

Acknowledgements

This work was supported by the National Key R&D Program of China (Grant No. 2024YFA1409200), the National Natural Science Foundation of China (Grant Nos. 12595332 and 11974394), the Chinese Academy of Sciences (CAS) Project for Young Scientists in Basic Research (Grant No. YSBR-057), the Synergetic Extreme Condition User Facility (SECUF), and the Scientific Instrument Developing Project of CAS (Grant No. ZDKYYQ20210003).

References

[1] Nagaosa N, Sinova J, Onoda S, MacDonald A H and Ong N P 2010 *Rev. Mod. Phys.* **82** 1539
[2] Pugh E M 1930 *Phys. Rev.* **36** 1503
[3] Pugh E M and Lippert T W 1932 *Phys. Rev.* **42** 0709
[4] Manna K, Muechler L, Kao T H, Stinshoff R, Zhang Y, Gooth J, Kumar N, Kreiner G, Koepernik K, Car R, Kübler J, Fecher G H, Shekhar C, Sun Y and Felser C 2018 *Phys. Rev. X* **8** 041045
[5] Manna K, Sun Y, Muechler L, Kübler J and Felser C 2018 *Nat. Rev. Mater.* **3** 244
[6] Nakatsuji S, Kiyohara N and Higo T 2015 *Nature* **527** 212
[7] Nayak A K, Fischer J E, Sun Y, Yan B H, Karel J, Komarek A C, Shekhar C, Kumar N, Schnelle W, Kubler J, Felser C and Parkin S S P 2016 *Sci. Adv.* **2** 1501870
[8] Karplus R and Luttinger J M 1954 *Phys. Rev.* **95** 1154
[9] Kooi C 1954 *Phys. Rev.* **95** 843
[10] Smit J 1958 *Physica* **24** 39
[11] Smit J 1955 *Physica* **21** 877
[12] Berger L 1970 *Phys. Rev. B* **2** 4559
[13] Chen B W and Shen B 2024 *Chin. Phys. B* **33** 087501
[14] Xiao D, Chang M C and Niu Q 2010 *Rev. Mod. Phys.* **82** 1959
[15] Behnia K 2009 *J. Phys. Condens. Mat.* **21** 113101
[16] Behnia K and Aubin H 2016 *Rep. Prog. Phys.* **79** 046502
[17] Xiao D, Yao Y G, Fang Z and Niu Q 2006 *Phys. Rev. Lett.* **97** 026603
[18] Burkov A A 2014 *Phys. Rev. Lett.* **113** 187202
[19] Burkov A A 2018 *Annu. Rev. Conden. Ma. P.* **9** 359
[20] Nagaosa N, Morimoto T and Tokura Y 2020 *Nat. Rev. Mater.* **5** 621
[21] Liu E K, Sun Y, Kumar N, Muechler L, Sun A L, Jiao L, Yang S Y, Liu D F, Liang A J, Xu Q N, Kroder J, Suss V, Borrmann H, Shekhar C, Wang Z S, Xi C Y, Wang W H, Wirth S, Chen Y L, Goennenwein S T B and Felser C 2018 *Nat. Phys.* **14** 1125
[22] Guin S N, Vir P, Zhang Y, Kumar N, Watzman S J, Fu C G, Liu E K, Manna K, Schnelle W, Gooth J, Shekhar C, Sun Y and Felser C 2019 *Adv. Mater.* **31** 1806622
[23] Belopolski I, Manna K, Sanchez D S, Chang G Q, Ernst B, Yin J X, Zhang S S, Shumiya N, Zheng H, Singh B, Bian G, Multer D, Litskevich M, Zhou X T, Huang S M, Wang B K, Chang T R, Xu S Y, Bansil A, Felser C, Lin H and Hasan M Z 2019 *Science* **365** 1278
[24] Guin S N, Manna K, Noky J, Watzman S J, Fu C G, Kumar N, Schnelle W, Shekhar C, Sun Y, Gooth J and Felser C 2019 *NPG Asia Mater.* **11** 16
[25] Rai B K, O'Rourke P and Roy U N 2022 *J. Phys. Condens. Mat.* **34** 273002
[26] Singh A K, Sarkar S and Peter S C 2022 *Chem. Rec.* **22** e202100317
[27] Essafi K, Jaubert L D C and Udagawa M 2017 *J. Phys. Condens. Mat.* **29** 315802
[28] Bolens A and Nagaosa N 2019 *Phys. Rev. B* **99** 165141
[29] Sun Z Y, Zhou H, Wang C X, Kumar S, Geng D Y, Yue S S, Han X, Haraguchi Y, Shimada K, Cheng P, Chen L, Shi Y G, Wu K H, Meng S and Feng B J 2022 *Nano Lett.* **22** 4596
[30] Li M, Ma H, Lou R and Wang S C 2025 *Chin. Phys. B* **34** 017101
[31] Bie H Y, Zelinska O Y, Tkachuk A V and Mar A 2007 *Chem. Mater.* **19** 4613
[32] Bud'ko S L, Huyan S Y and Canfield P C 2026 *Phys. Rev. B* **113** 014431
[33] Li L F, Guan S Y, Chi S W, Zhao J Z, Li J W, Lin X X, Xu G and Jia S 2026 *Sci. Bull.* **04** 027

[34] Lin X, Taufour V, Bud'ko S L and Canfield P C 2013 *Phys. Rev. B* **88** 094405

[35] Lemoine P, Cadogan J M, Slater B R, Mar A and Avdeev M 2013 *J. Magn. Magn. Mater.* **325** 135

[36] Tian Y, Ye L and Jin X F 2009 *Phys. Rev. Lett.* **103** 087206

[37] Onoda S, Sugimoto N and Nagaosa N 2006 *Phys. Rev. Lett.* **97** 126602

[38] Miyasato T, Abe N, Fujii T, Asamitsu A, Onoda S, Onose Y, Nagaosa N and Tokura Y 2007 *Phys. Rev. Lett.* **99** 086602

[39] Sun P J, Kumar K R, Lyu M, Wang Z, Xiang J S and Zhang W Q 2021 *The Innovation* **2** 100101

[40] Ikhlas M, Tomita T, Koretsune T, Suzuki M T, Nishio-Hamane D, Arita R, Otani Y and Nakatsuji S 2017 *Nat. Phys.* **13** 1085

[41] Watzman S J, Duine R A, Tserkovnyak Y, Boona S R, Jin H, Prakash A, Zheng Y H and Heremans J P 2016 *Phys. Rev. B* **94** 144407

[42] Ramos R, Aguirre M H, Anadón A, Blasco J, Lucas I, Uchida K, Algarabel P A, Morellón L, Saitoh E and Ibarra M R 2014 *Phys. Rev. B* **90** 054422

[43] Lyu M, Liu J Y, Zhang S, Liu Y, Yang J Y, Wang Y B, Feng Y T, Wang B B, Wei H X and Liu E K 2025 *Phys. Rev. B* **111** 014424

[44] Lyu M, Liu J Y, Shen J L, Zhang S, Liu Y, Yang J Y, Wang Y B, Feng Y T, Wang B B, Wei H X and Liu E K 2025 *Adv. Sci.* **12** 2411702

[45] Xu L C, Li X K, Ding L C, Chen T S, Sakai A, Fauqu B, Nakatsuji S, Zhu Z W and Behnia K 2020 *Phys. Rev. B* **101** 180404

[46] Li X K, Xu L C, Ding L C, Wang J H, Shen M S, Lu X F, Zhu Z W and Behnia K 2017 *Phys. Rev. Lett.* **119** 056601